The crystallographic structure of the air-grown oxide on depleted uranium metal

Christopher P. Jones*[a], James R. Petherbridge[b], Sean A. Davis[c], Jonathon A. Jones[c], Thomas B. Scott[a],

[a] *Interface Analysis Centre, HH Wills Physics Laboratory, Tyndall Avenue, Bristol, BS8 1TL, UK* * *corresponding author cj0810@bristol.ac.uk*
[b] *AWE, Aldermaston, Reading, Berkshire, RG7 4PR, UK*
[c] *School of Chemistry, University of Bristol, Cantock's Close, Bristol, BS8 1TS, UK*

Abstract

Oxide formation on depleted uranium metal was investigated using a combination of electron backscatter diffraction (EBSD) and transmission electron microscopy (TEM) characterisation. Diffraction analysis of the oxide revealed an FCC crystalline formation of UO_2 crystallites whilst TEM data indicated an average grain size of 12 nm with a standard deviation of 3.8 nm. EBSD analysis revealed a preferential texture of [110] normal to the surface of the metal. This data implied that lattice matching between the oxide and the underlying metal did not occur, therefore, the observed preferential growth direction is independent of the underlying crystal orientation.

Keywords: B. SEM, B. STEM, B. TEM, C. atmospheric corrosion, C. oxidation

1. Introduction

Understanding the factors which influence uranium corrosion is of relevance to a variety of industrial, environmental and academic activities. Of particular interest is the behaviour of uranium within long-term storage and disposal environments, i.e. in the presence of atmospheric gasses such as oxygen and water vapour.

A particular concern regarding the corrosion of uranium in humid environments is that when this occurs in a sealed container the reaction will consume oxygen [1]. If the oxygen level is sufficiently reduced then the water-uranium reaction produces hydrogen, thus potentially forming pyrophoric uranium hydride. However, the initiation of uranium hydride reaction sites has been shown to be strongly dependent on the characteristics (e.g. thickness) of the surface uranium oxide layer present on the uranium metal [2–6].

The clear influence that the uranium surface oxide layer has on hydride site initiation has led to the development of mathematical models which assume that site nucleation is controlled by the transport of hydrogen through the oxide to the underlying metal. The model put forward by Y Ben Eliyahu and co-workers [7] assumes that hydride reaction sites are limited to a maximum concentration for a given uranium surface. In contrast, Glascott proposed a model in which there is a distribution of oxide layer thickness across the uranium surface which leads to a variation in the observed number of hydride reaction sites with time [8].

It is, therefore, evident that characterisation of the air grown surface oxide layer on uranium (i.e. crystallite size and orientation) would further the mechanistic understanding of uranium corrosion, both in relation to the reaction with moist air and also with hydrogen.

The rate and mechanism of the reaction of uranium with oxygen and water has been studied with each gas in isolation and also for mixtures of the two gasses [2, 9–21]. These investigations utilised techniques such as gas consumption [9], mass gain analysis [13, 15], ellipsometry measurements [10, 17, 18] Raman spectroscopy[19], X-ray photoelectron spectroscopy [20] and infra red spectroscopy[21]. Thus, few studies have been reported regarding the characterisation of the structure of air-grown uranium oxide film on a sub-μm scale.

However, an early X-ray diffraction (XRD) study by Waber *et al.* [22] reported that uranium dioxide formed by the reaction of uranium with water vapour occurs with a distinctive growth habit. The (110) planes of the dioxide were reported to lie parallel to the surface of the uranium substrate. Furthermore, no evidence was found for an epitaxial relationship between the metal and the oxide.

A subsequent XRD and electron diffraction study carried out by, Bessonov *et al.* [23] concluded that the oxide film formed on uranium samples by air exposure at room temperature was UO_2, with a lattice parameter a = 0.545 nm. Furthermore, the oxide was stated as having a polycrystalline

structure with broadening of the XRD spectra indicating a crystallite size of approximately 10^{-4} cm (i.e. $\sim$1 μm). Similar XRD measurements have since been reported by Chernia and co workers [21], giving an oxide crystallite size of 15 nm for a 270 nm thick oxide grown at 160 °C in oxygen. Furthermore, an oxygen-anion hopping mechanism was proposed to account for the observed preferred growth in the [110] direction.

Theoretical work by Tasker [24] calculated the surface energy, tension and structure of the low index faces of uranium dioxide using an ionic description of the crystal formation. The <111> orientation exhibited the lowest surface energy, however, the individual planes are charged since they consist of only one ion type (either uranium or oxygen). Whilst for the <110> orientation the surface energy is higher but individual planes of atoms are charge neutral, consisting of a mix of uranium and oxygen atoms making this the favourable growth direction.

From the discussion presented above it is clear that no direct observations have been reported of the microstructural configuration of uranium oxide forming on metal surfaces. Therefore the current work utilised focused ion beam (FIB) to prepare cross-sections through the surface of deliberately oxidised samples. Transmission electron microscopy (TEM), scanning TEM (STEM) and scanning electron microscopy (SEM) methods were employed to directly image the oxide layer to determine crystallite size. In addition, TEM and electron backscatter diffraction (EBSD) provided complimentary data by confirming the crystalline structure and orientation of the oxide overlayer. Particular attention was devoted to identifying a relationship, or lack thereof, between the crystal orientation of the exposed metal surface and the growth direction of the formed oxide layer.

2. Experimental Method

2.1. Initial surface preparation and oxidation

The current study utilised two types of depleted uranium samples, referred to as low carbon (<100 ppm) and high carbon (600 ppm). The low carbon samples were identical to those used in a previous study [25], i.e. 10 mm square, $\sim$1 mm thick, with a grain size of $\sim$15 μm. Chemical analysis of samples from the same source yielded impurity levels for iron, aluminium, silicon and chromium of 22, $\sim$5, $\sim$2 and $\sim$2 ppm (by weight), respectively [6]. These samples were obtained from rolled feedstock and annealed for 164 hrs, at 550 °C under vacuum at $<1\times10^{-4}$ Pa, prior to further preparation.

The high carbon samples were in the form of disks (15 mm diameter, 1 mm thick) cut from a cast rod. These samples were identical to those used in a previous studies [26, 27]. In general, higher impurity levels were present within the high-carbon samples as compared to the low-carbon samples, with analysis of material from the same source as the high-carbon samples indicating levels for iron, aluminium, silicon and chromium of ∼140, ∼40, ∼130 and ∼20 ppm (by weight) respectively [28]. Prior analysis of the microstructure of the samples indicated a coarsely grained texture typical of cast metal, with large grains frequently >100 μm in width, with long, relatively straight, low angle (<25 °) grain boundaries and occasional sets of well defined crystal twins.

In each instance the metal coupon surfaces were prepared in the open laboratory using wet mechanical polishing. Samples were abraded using water as a lubricant on Buehler SiC paper of increasingly fine grade (from P600 to P2500) in a process designed to minimise the work hardening effect on the bulk metal. The surfaces were then lapped using a 1 μm diamond paste on a short nap cloth, then rinsed in ethanol and dried in air.

Controlled surface oxidation was performed upon two coupons (one of each purity) in the open laboratory at room temperature and pressure for a duration of 42 days, the oxides formed in this manner were the primary focus of the TEM investigation. In order to form a substantial oxide layer several microns in thickness, four coupons (two samples of each purity) were oxidised in a conventional oven for 12 hrs at 150 °C. One low carbon and one high carbon sample were then retained for TEM/STEM analysis while the remaining samples were prepared for EBSD analysis.

2.2. Sample preparation for TEM analysis

In-situ TEM sections were prepared from both purities of uranium metal following oxide growth at room temperature and 150 °C. A platinum coating was deposited prior to ion beam milling, in order to protect the oxide surface. A Helios X600 Dualbeam system was used to cut 10×5×1 μm sections of material from the surface, and a kleindike nanomanipulator needle was used to extract the cut sections. After controlled ion beam milling to form a TEM section 1 μm thick, the nanomanipulator needle was attached via further controlled platinum deposition and the section was cut and lifted free. Once removed, the 1 μm thick slice was positioned over a half-moon shaped TEM grid and attached using platinum deposition. The sample was then thinned, in-situ, to a thickness of 50-100 nm and following STEM imaging at 30 kV

transferred to the TEM system. TEM analysis of samples was performed on a Jeol 2010 transmission electron microscope; for image and diffraction pattern collection a Gatan Orius SC 1000 camera was used. Spot diffraction was obtained at 300× magnification with a 1 nA probe current, a 2 second dwell time and a 200 nm selected area aperture.

2.3. Sample preparation for EBSD analysis

EBSD analysis currently requires a minimum grain size of 50 nm in order to produce measurable kikuchi bands for computational analysis. Therefore, samples with the thick oxide layer (>5 μm) formed at 150 °C were heated to 550 °C under UHV conditions for 12 hrs in order to anneal the sample and induce grain growth. The annealed microstructure will therefore differ from an ambient formed oxide, however, in terms of crystallographic orientation, the annealed oxide is likely to be sufficiently representative of the air grown oxide to determine if there exists a preferred crystal orientation in relation to the underlying parent metal grains.

The annealed samples were loaded into an FEI FIB201 focused gallium ion beam instrument for grazing-angle etching, producing a section through both the oxide and the underlying metal. Samples were ion etched at a 10 ° angle parallel to the surface, at the maximum probe current of 11.5 nA, to produce a surface suitable for EBSD mapping. A shallow etching angle is required to produce surface architecture that would allow diffracted electrons to reach the detector. An additional benefit of utilising an acute angle through the oxide (as opposed to etching to the surface normal) is an increase in the surface area of exposed oxide available to be mapped.

After preparation in the FIB, the samples were transferred into a Zeiss EVO MA10 equipped with LaB_6 electron source and TSL-EDAX instrumentation, for crystallographic electron backscatter diffraction mapping (EBSD) of the etched areas. EBSD data were recorded using OIM^{TM} software for both data capture and analysis. The metal was mapped using structural data provided from the standard TSL database for orthorhombic α-uranium, whilst the oxide was mapped using the structural data for UO_2. Where necessary, the raw EBSD data recorded during mapping runs were cleaned using standard OIM^{TM} clean-up functions (nearest neighbour correlation and grain dilation functions).

3. Results and Discussion

3.1. STEM/TEM analysis of the surface formed oxide

3.1.1. Low Carbon Uranium

Figure 1a) shows an acquired STEM image of a cross-sectional specimen extracted from the top 10 μm of a low carbon sample that had been exposed to ambient conditions for 42 days, whilst b) shows the individually identified grains outlined in red which were subsequently analysed to obtain grain diameter measurements. A total of 46 grains were analysed with the average internal diameter being determined for each, this resulted in a range from 6.8 to 21.9 nm. The mean of the average internal diameters was calculated to be 13.2 nm, with standard deviation (σ) of 4.2 nm. Similar analysis was conducted using TEM acquired images (figure 2), captured from the same sample but obtained from different regions of the oxide layer. This second analysis revealed an average internal diameter of 11.7 nm with a standard deviation (σ) of 2.9 nm across the 23 identified grains.

Only the grain boundaries which were clearly defined were analysed to avoid incorrectly inferring the average grain size from overlapping grains. It was impossible to avoid the situation of grain overlap due to their nanometer size. Therefore, sections were cut as thinly as possible ($\sim$50 nm) in order to produce the highest quality images with minimal overlap of grains, however, there will always be limitations of this technique at these length scales.

Spot diffraction analysis of the oxide confirmed the expected FCC structure with a measurement of the lattice parameter to be 0.524 nm(figure 3). Additionally, oxides formed over 8 hours at 150 °C exhibited ostensibly identical structure with a measured lattice parameter of 0.557 nm (Figure 4). In each case the use of a 200 nm aperture resulted in sampling of approximately 400-500 grains, therefore, any localised effects will significantly alter measurements of lattice spacing.

Figure 5 shows a high resolution TEM image of the oxide:metal interface, with lattice fringes within the oxide clearly observed at an angle of approximately 40 ° to the plane of the metal surface. The insert to figure 5 displays the corresponding fast Fourier transformation (FFT). The lattice fringes exhibited a spacing of 0.316 nm matching closely to the reference value of the [111] lattice planes for the FCC, UO_2, structure giving a lattice parameter measurement of 0.547 nm. This differs slightly from the diffraction measurement of lattice parameter (0.524 nm) from the same sample albeit a different

region and is likely due to localised effects such as stress and variation in stoichiometry.

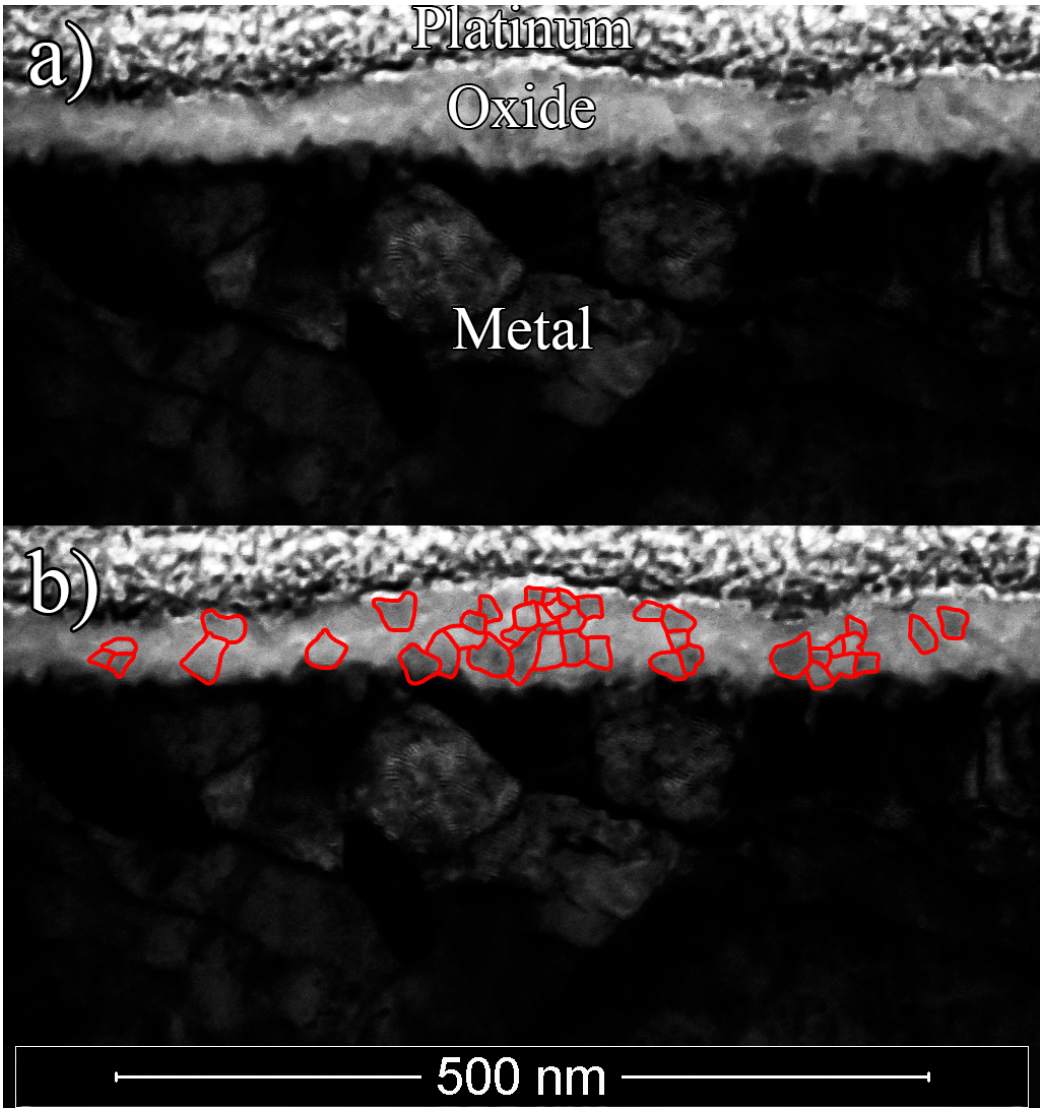

Figure 1: a) section removed from a low carbon sample exposed to ambient conditions for 42 days. The image shows (from top to bottom) the Pt layer deposited prior to section preparation, the oxide layer and underlying metal. b) presents a duplicate STEM image with a red overlay designating the individual grains for measurement and analysis (mean diameter of 13.2 nm with $\sigma = 4.2$ nm).

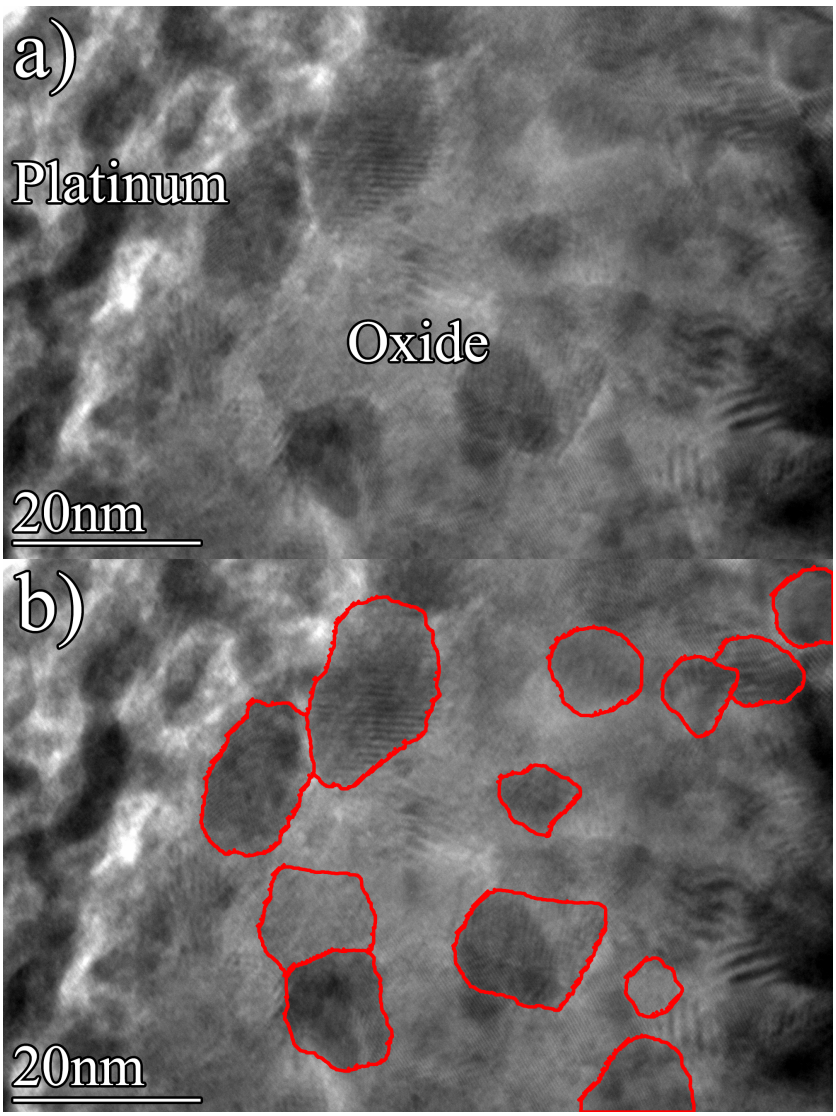

Figure 2: a) TEM image of the oxide formed on low carbon uranium following 42 days exposure to ambient environmental conditions. b) TEM image with a red overlay designating the individual grains for measurement and analysis (mean diameter of 11.7 nm with σ = 2.9 nm). The two grains that intersect with the edge of the image were not included in this analysis

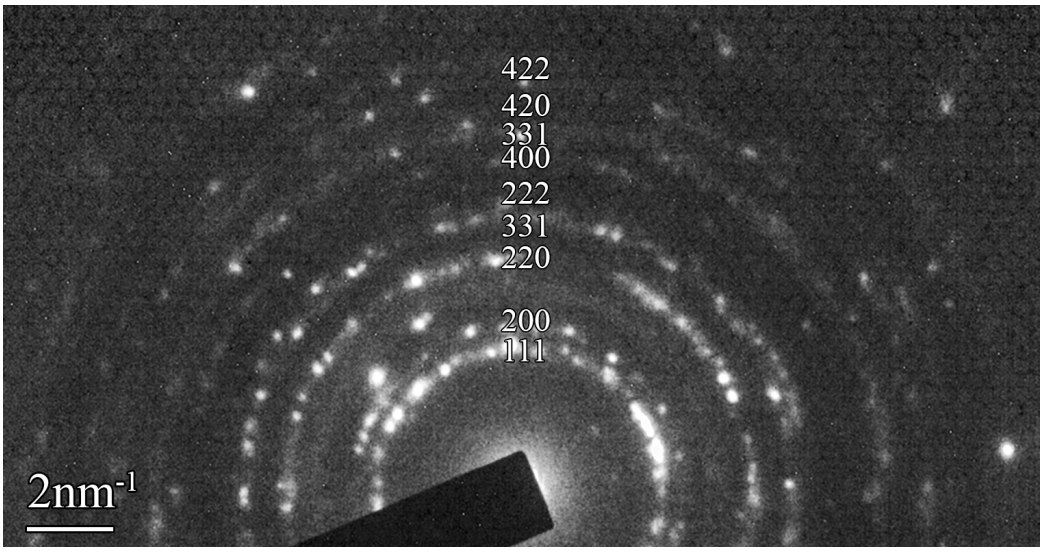

Figure 3: Diffraction pattern from the oxide formed on low carbon uranium after 42 days in air. The diffraction rings correspond to reflections from the UO_2 FCC lattice, albeit with a measured lattice parameter of 0.524 nm.

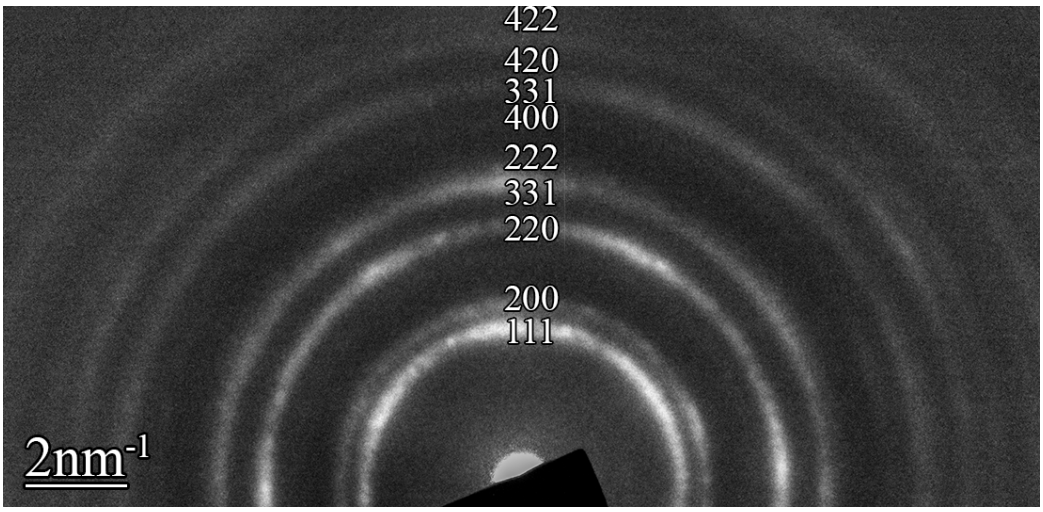

Figure 4: Diffraction pattern from the oxide formed on low carbon uranium after 8 hours oxidation at 150 °C. The diffraction rings correspond to reflections from the UO_2 FCC lattice, albeit with a measured lattice parameter of 0.557 nm.

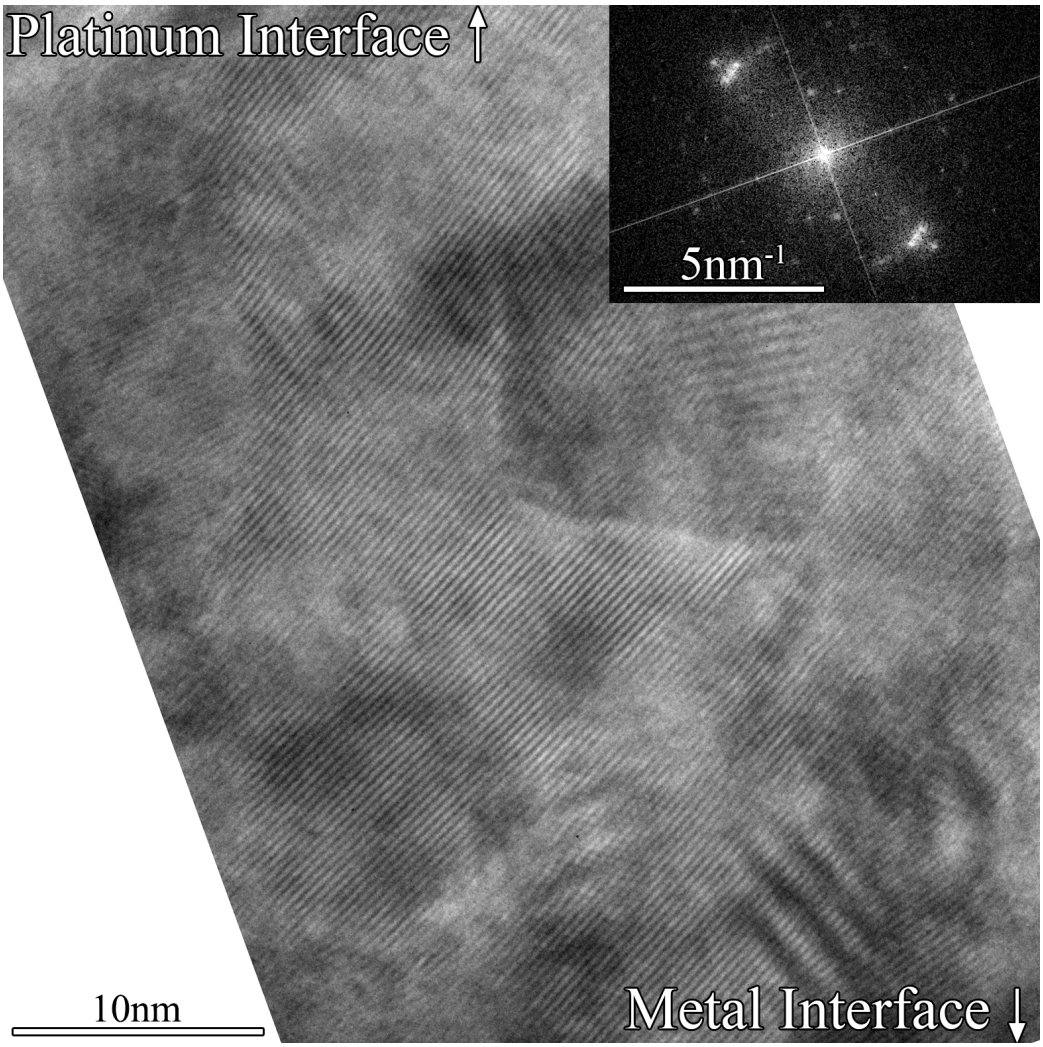

Figure 5: Bright-field TEM image of a section through an oxide formed over forty two days, at room temperature, on low carbon uranium metal, in air. The lattice fringes of the [111] planes are clearly oriented at 40 ° to the surface. The insert shows a fast Fourier transformation of the figure measuring the [111] lattice planes to exhibit a spacing of 0.316 nm.

3.1.2. High Carbon Uranium

There was little discernible variation in oxide grain size between the high and low carbon samples exposed to ambient conditions for 42 days. STEM analysis of a section from the high carbon sample (figure 6) yielded a mean for the average internal grain diameter of 12.7 nm (σ of 3.7 nm) with 75 grains analysed. Whereas TEM analysis of a different oxide region (figure 7) provided a mean and standard deviation of 11.9 and σ of 5.0 nm respectively with a sample size of 50.

Image acquisition was achieved at a higher magnification than the low carbon samples, however, the surface roughness appears greater. The sample will have inherent variation in surface topography due to mechanical polishing and the metal grain orientation. It is, however, unrealistic to infer a correlation between surface oxide roughness and impurity content since the analysis area is very small and, therefore, not representative of the surface as a whole.

Electron diffraction analysis of both high carbon samples was consistent with an FCC uranite structure (Figures 8 and 9) exhibiting a calculated lattice parameter of 0.536 nm and 0.541 nm respectively.

Figure 10 shows a high resolution TEM image of the oxide:metal interface, the lattice fringes are typically restricted to individual particles of 5-10 nm in diameter. These particles (and hence fringes) are not iso-oriented in this region but do lie at a preferred angle of 40-50 $^\circ$ to the plane of the metal surface. The FFT (figure 10 inset) confirms a lattice spacing of 0.32 nm consistent with the [111] planes of UO_2.

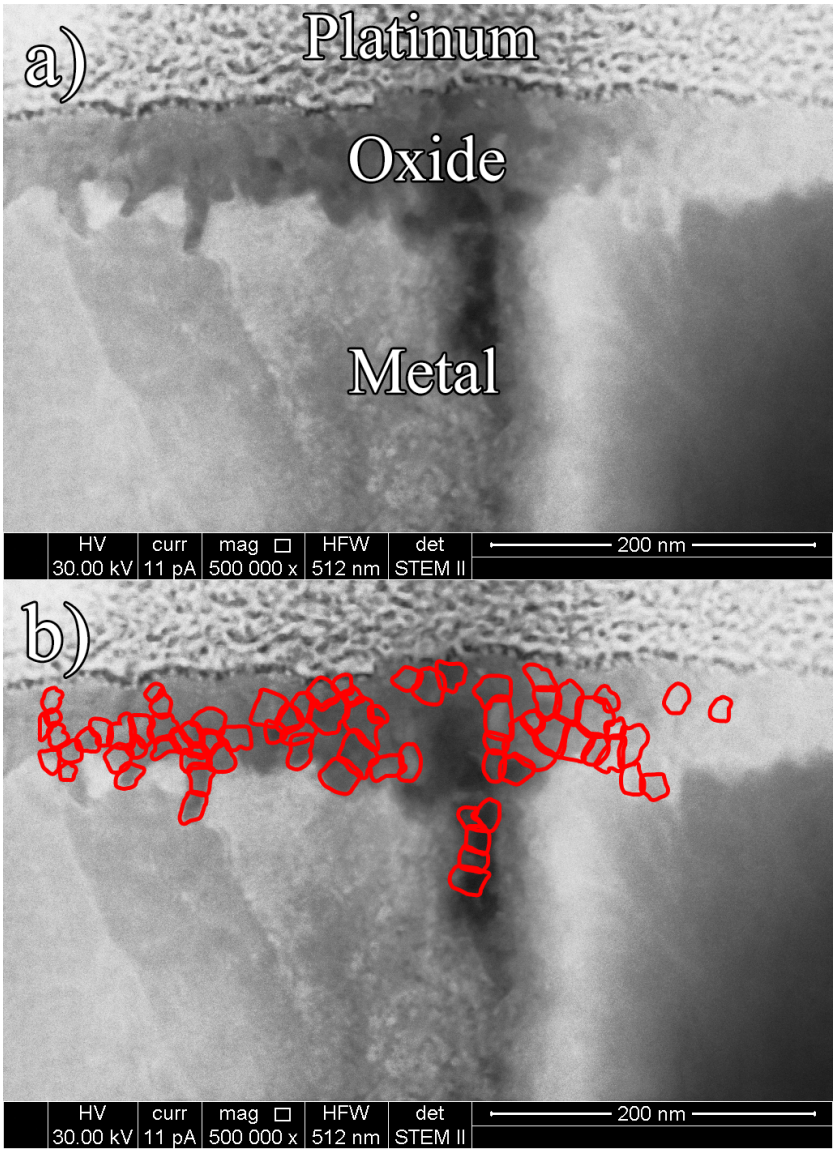

Figure 6: a) STEM image of the oxide formed on high carbon uranium following 42 days exposure to ambient environmental conditions. b) STEM image with a red overlay designating the individual grains for measurement and analysis (mean diameter of 12.7 nm with $\sigma = 3.7$ nm).

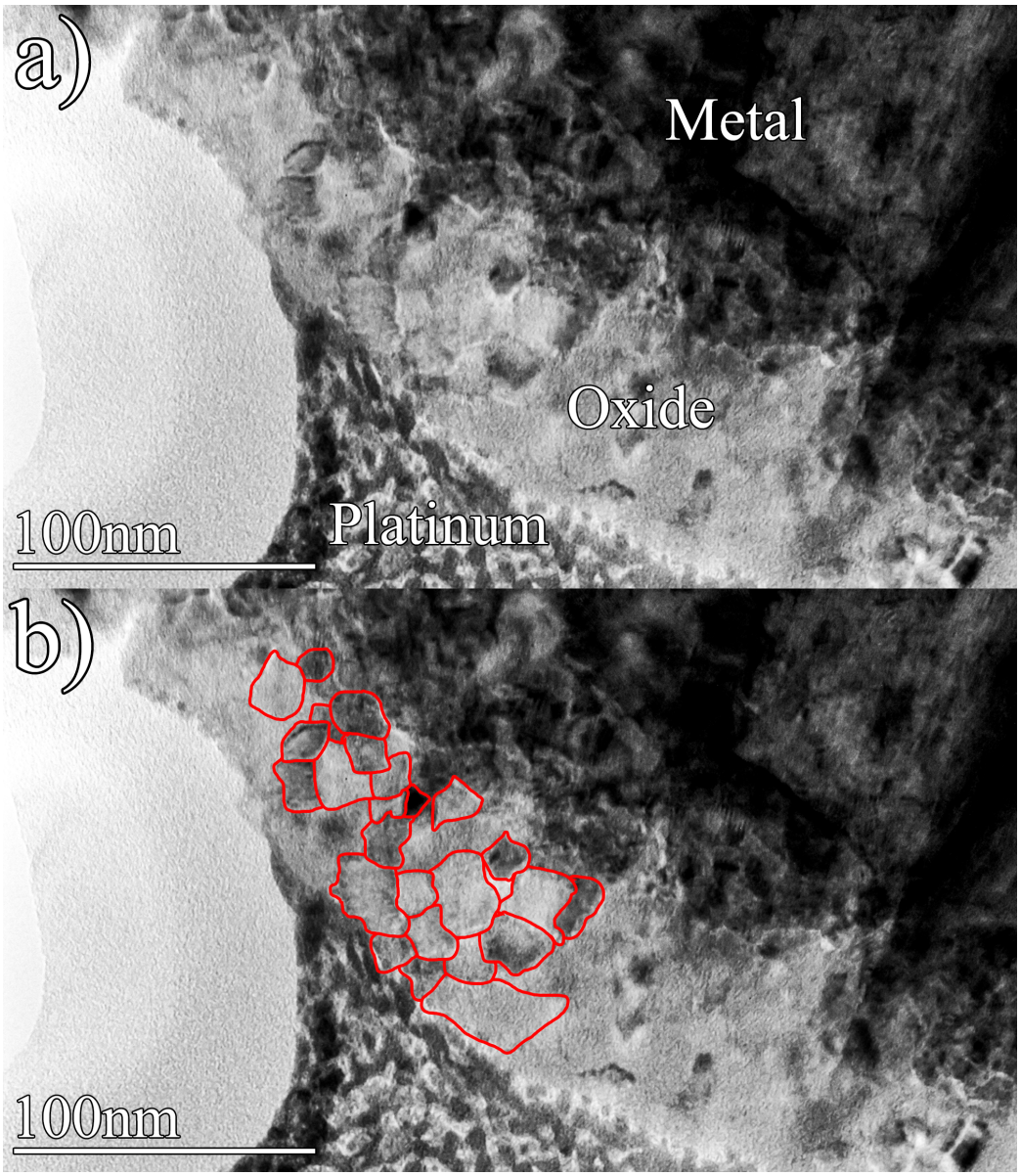

Figure 7: a) TEM image of the oxide formed on high carbon uranium following 42 days exposure to ambient environmental conditions. b) TEM image with a red overlay designating the individual grains for measurement and analysis (mean diameter of 11.9 nm with $\sigma = 5.0$ nm).

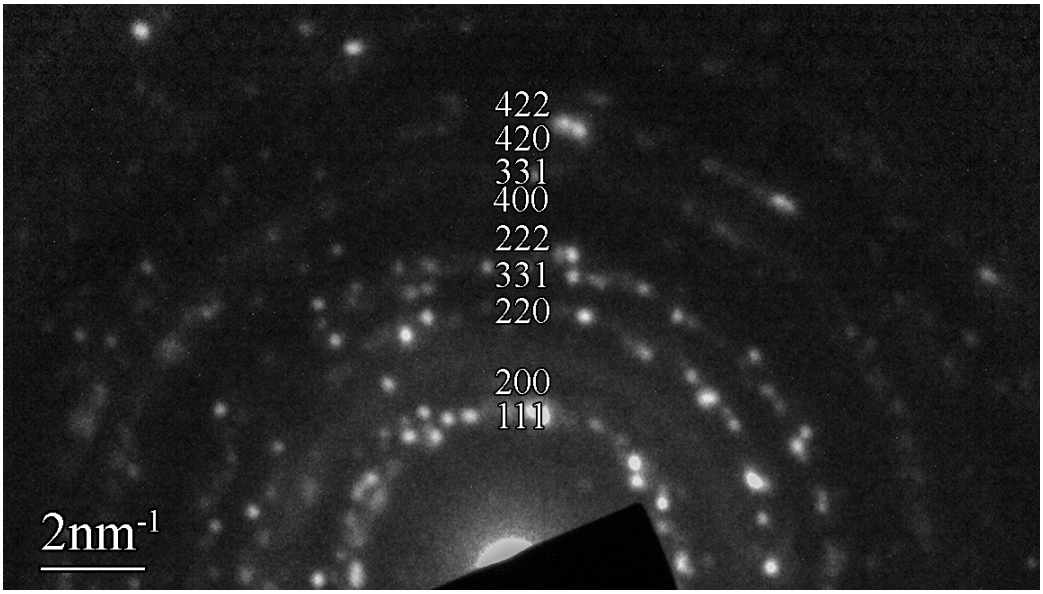

Figure 8: Diffraction pattern from the oxide formed on high carbon uranium after 42 days in air. The diffraction rings are consistent with the FCC structure of UO_2 albeit with a calculated lattice parameter of 0.536 nm

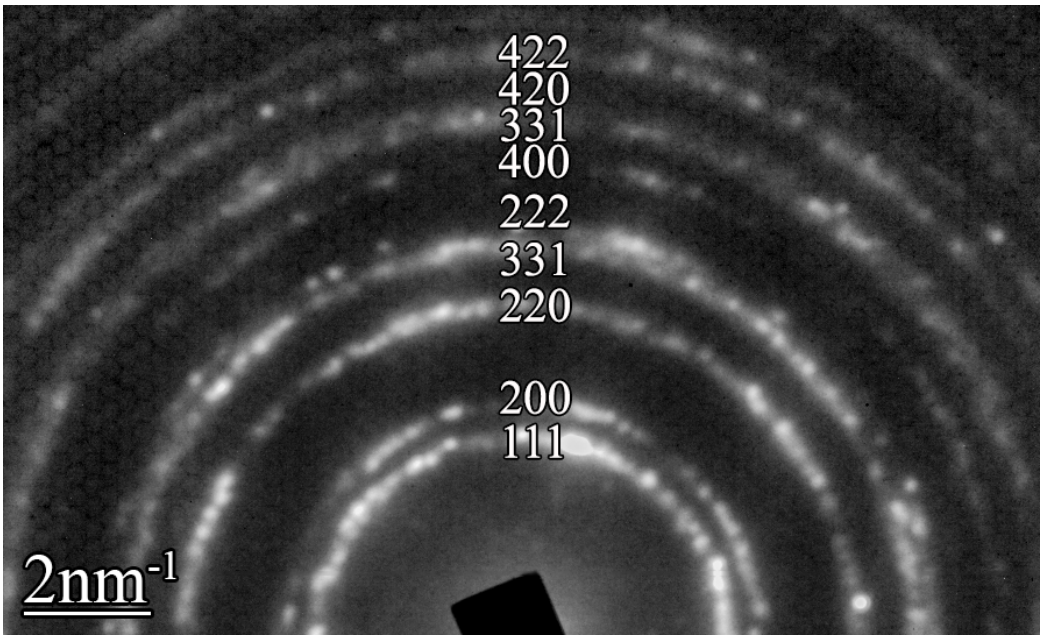

Figure 9: Diffraction pattern from the oxide formed on high carbon uranium at 150 °C after 8 hours growth. The diffraction rings correspond to the reflections from the UO_2 FCC lattice albeit with a calculated lattice parameter of 0.541 nm.

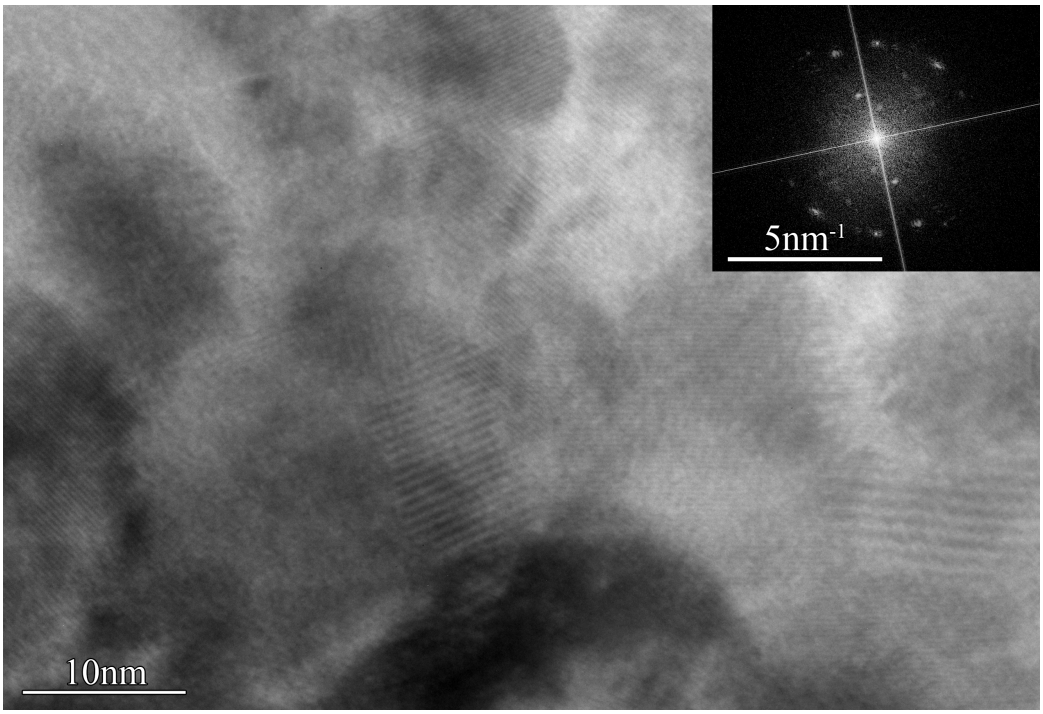

Figure 10: Bright-field TEM image of a section through an oxide formed over forty two days, at room temperature, on high carbon uranium metal, in air. The FFT confirms the lattice fringes are [111] lattice planes exhibiting a spacing of 0.32 nm and indicates a slight preferred orientation of $\sim$40-50 $^\circ$ to the metal surface.

3.2. EBSD analysis of the surface formed oxide

As discussed above, TEM analysis of the oxide formed at 150 °C and at room temperature indicated a range in grain sizes of 5-20 nm. EBSD analysis, however, requires a grain size in excess of 20 nm. Therefore, investigation of the surface oxide was only possible on samples that had been annealed at 550 °C in order to increase the size of UO_2 crystals prior to analysis.

As expected, the annealing process enlarged the average grain size without changing the overall preferred orientation previously found from x-ray diffraction measurements by Waber *et al.*[22].

To allow effective EBSD grain orientation mapping, surface ion beam sections were cut at 80 ° to the surface normal resulting in a smooth shallow plane at 10 ° through the oxide and into the metal below.

The EBSD analysis of an oxidised, annealed, low carbon uranium coupon is presented in figure 11 as a) an inverse pole figure map, which defines crystalline orientation, and b) as a phase map displaying the regions of metal (green) and UO_2 (red). The high resolution map (50 nm) indicated a topographic variation in the oxide-metal interface, evidenced by the regions of oxide located within the parent metal grain, taking into account the shallow angle of the cut-face. The EBSD data gathered from the oxide formed on low carbon uranium, across several grains, found a preferred crystallographic orientation thereby providing evidence that this growth direction is unrelated to that of the parent metal grain from which it was formed. Figure 12 presents an inverse pole figure plot, and corresponding textures plots from the EBSD analysis showing the distribution of crystalline orientations. From this is is deduced that the oxide forms with a preferred orientation in the [110] direction at a frequency 3.6 times that of a random direction.

Figure 13 displays the EBSD data collected from the high carbon sample, presented as a) an inverse pole map and b) a phase map of a perpendicular section cut into the surface oxide. A large proportion of the oxide layer does not produce diffraction patterns and was evident in the form of elliptical areas with an absence of signal. It is known from previous work by Orlov *et al.* [29] that annealing at high temperature promotes carbon migration to the surface of the metal. Figure 14 shows secondary ion mass spectrometry analysis of a high-carbon sample following an annealing treatment (550 °C, 48 hours) comparable to that utilised in the current study. The presence of carbon rich features surrounded by oxygen rich areas (i.e. oxide) is clearly indicated. In addition, limited signal due to oxygen is also obtained from the carbon-rich features, thus suggesting that the areas from which EBSD

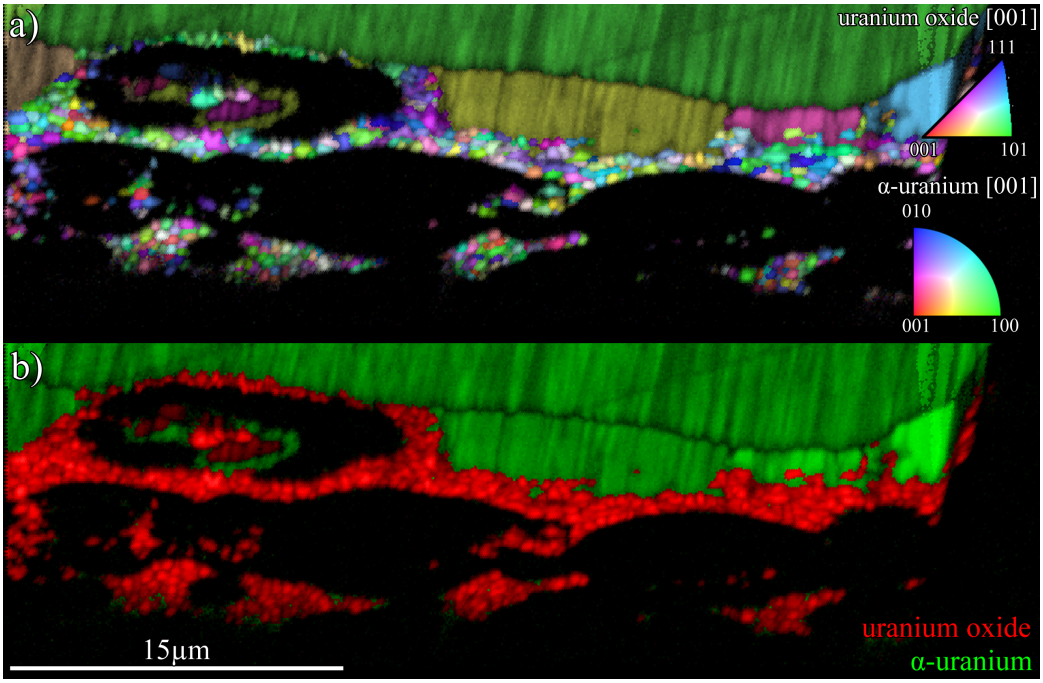

Figure 11: EBSD analysis on a surface cut at an incident angle of 10 ° parallel to the surface on low carbon depleted uranium metal. The oxide layer was formed at 150 °C with further annealing under high vacuum at 550 °C. The analysis presented shows a) a colour representation inverse pole figure map overlaid with a grey-scale secondary electron (SE) data, and b) an SE image with false colouring to indicate the phases present in the material. The data is presented as-received, therefore while the x-axis scale-bar is accurate, the actual size of crystalline grains in the y-direction is 5 times smaller due to the scanning angle.

patterns were not obtained in figures 13 and 11 are ascribed to the formation of a uranium oxycarbide compound.

Figure 15 presents an inverse pole figure plot, and corresponding textures plots from figure 13 showing the distribution of crystalline orientations. The preferred orientation is also towards the [110] direction, however, unlike the low carbon, the frequency is far higher at ∼7.3 times that of a random direction.

The EBSD maps presented in figure 13 measured an average oxide grain size of a few hundred nanometres after the high temperature annealing. The 100 μm FIB cut through the oxide was found to intersect a single metal

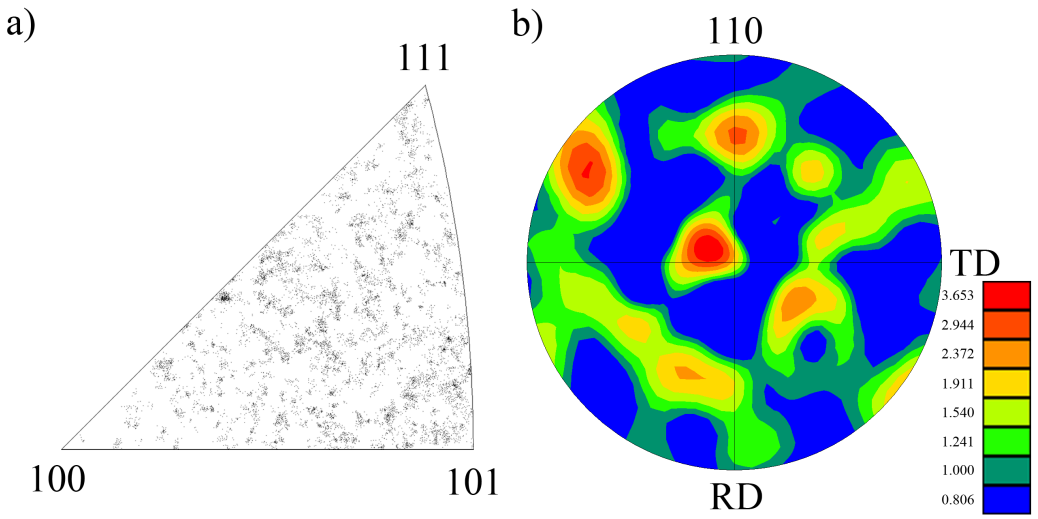

Figure 12: a) Inverse pole figure plot of the uranium oxide phase grown on low carbon uranium from figure 11 the trend towards the [110] direction is not clearly observed, however, the pole figure texture plot (b) shows the extent of the preferred [110] direction within the uranium oxide grains mapped in figure 11. The scalebar shows the frequency of grain orientations within the binned contour regions.

grain upon which the oxide had formed. This was to be expected since the crystalline grain size for this material extended up to millimeters in diameter.

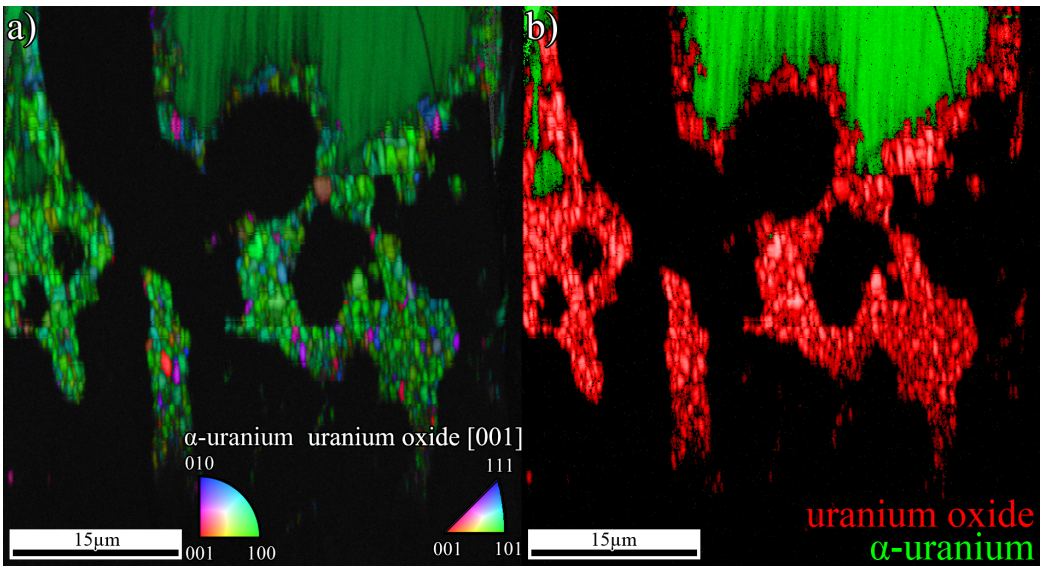

Figure 13: EBSD analysis on a surface FIB cut at an incident angle of 10 ° parallel to the surface on high carbon depleted uranium metal. The oxide layer was formed at 150 °C with further annealing under high vacuum at 550 °C. The analysis presented shows a) a colour representation inverse pole figure map overlaid with a greyscale secondary electron (SE) data, and b) an SE image with false colouring to indicate the phases present in the material. The data is presented as-received, therefore while the x-axis scale-bar is accurate, the actual size of crystalline grains in the y-direction is 5 times smaller due to the scanning angle.

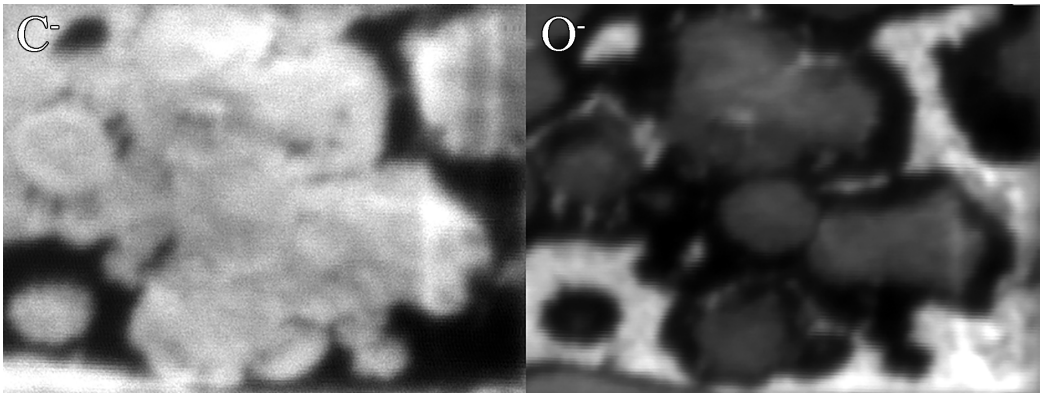

Figure 14: Negative SIMS ion maps cor C^- and O^- (as indicated of the surface of a high-carbon uranium sample following annealing at 550 °C for 48 hours.

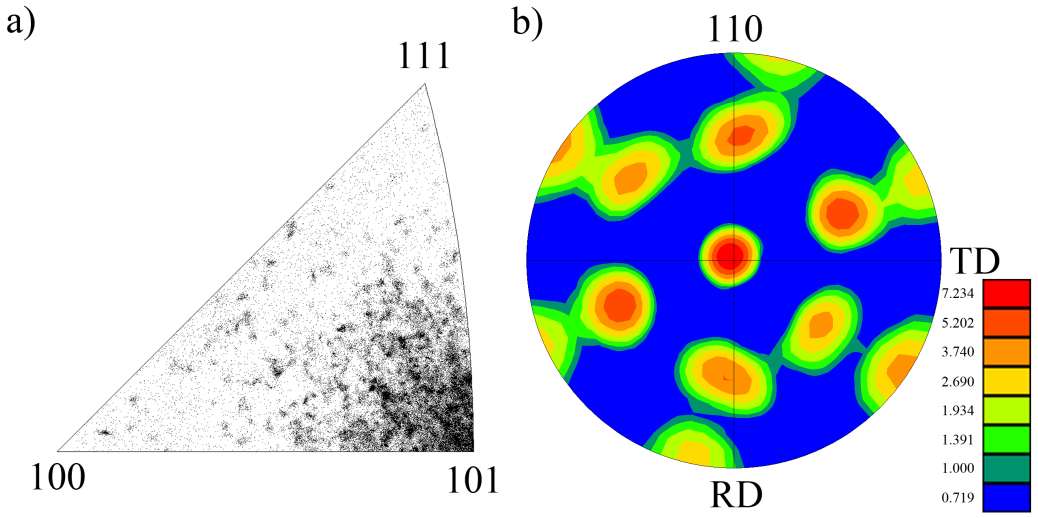

Figure 15: a) Inverse pole figure plot of the uranium oxide phase grown on high carbon uranium from figure 13 showing the trend towards the [110] direction. b) a pole figure texture plot showing the extent of the preferred [110] direction within the uranium oxide grains mapped in figure 13. The scalebar shows the frequency of grain orientations within the binned contour region.

3.3. Summary of oxide characterisation

EBSD data has revealed microstructural information regarding the oxide forming on uranium metal. In particular the crystallographic orientation of the oxide formation is apparently not influenced by the orientation of the underlying metal grains upon which they form. Instead, the oxide grows with a preferred orientation towards the [110] direction relative to the exposed metal surface, in agreement with the x-ray diffraction observations of Waber *et al*[22]. This was more apparent on the high carbon sample with a preference to orient along the (110) plane 7 times more often than that of a random direction (compared to 3.6 for the low carbon analysis) (Figures 15 and 12 respectively). The STEM/TEM analysis on both the high carbon and low carbon materials grown at room temperature revealed an oxide layer comprising of a polycrystalline matrix with individual grains ranging in size from 5-20 nm diameter and averaging 12.6 nm ($\sigma = 4.0$) from a total sample size of 192 identified grains. There was no observable difference between the grain size observed for oxides grown, at room temperature, from the two different purities of uranium metal. In addition, the oxide grain sizes measured directly via TEM analysis for all samples were found to be in good agreement with the crystallite size measured via XRD by Chernia and co workers [21], i.e. 15 nm for an oxide grown in oxygen on uranium at 160 °C.

The TEM diffraction analysis confirmed a uranite FCC structure typically matching to within 0.3 % of expected ratios (figure 8 matched to within 2.5 % due to the quality of diffraction patterns attained). The lattice parameter was found to be 0.54 nm varying by ± 0.02 nm depending on the analysis region. Reference literature values taken from X-ray bulk powder diffraction sit within this range at a value of 0.547 nm. The variation is likely due to the small area probed in the current study, i.e. because only a few grains are analysed factors such as stoichiometry, localised strain and crystallite size may each contribute to variations in the lattice parameter

Typically FCC oxides of metals with no lattice matching will grow with a preferred (111) orientation as it is the most energetically favourable, forming the closest packed structure. However, the oxide was observed to form with a (110) texture which is, therefore, a more energetically favourable system than if the growth direction was along the close packed (111) orientation. It is expected that this lower energy formation is due to the arrangement of uranium to oxygen atoms forming a charge neutral surface [30, 31].

4. Conclusions

Direct STEM and TEM imaging of the uranium oxide microstructure, formed in air, has revealed consistent characteristics for samples of both high and low carbon and also oxidation at RT and 150 °C, i.e. a polycrystalline structure with preferred grain orientation comprising of grains ranging in size from 5-20 nm and averaging 12.6 nm across the sampled data. This result implies that gaseous diffusion models, in particular hydrogen with its typically high diffusivity coefficient [32], should consider transport mechanisms via both the oxide lattice and the high density of grain boundaries.

In terms of the Glascott [8] and Ben-Eliyahu [7] models discussed in the introduction, both of these approaches consider the diffusion of hydrogen through a surface oxide layer to the underlying metal in terms of a single diffusion coefficient. In both cases neither the structure of the oxide nor the exact hydrogen diffusion paths are defined. The current work has shown the oxide layer is polycrystalline with a 10 - 20 nm grain size, thus indicating that hydrogen diffusion can occur via both the oxide grains themselves and the boundaries between them. However, these two contributions will still yield a single overall "effective" diffusion coefficient. Therefore, the assumptions of both the Glascott and Ben-Eliyahu models are consistent with the conclusions of the current study.

There was no observable evidence of any correlation between the crystallographic growth direction of the surface oxide film and the crystalline orientation of the underlying metal. Instead the surface oxide was found to exhibit a crystallographic growth preference towards a surface plane of (110) orientation as determined by EBSD analysis.

TEM diffraction analysis was employed to confirm that the oxide structure consisted of predominantly uranite with an FCC unit cell, this was achieved with a high degree of certainty. In addition, the measured lattice parameter was measured to be 0.54 $\pm$0.02 nm which likely varies due to the small analysis area encompassing only a few UO_2 grains taken at the surface of the material (when compared with traditional bulk XRD analysis). More detailed analysis on exact oxygen stoichiometry and/or strains is beyond the scope of the current investigation and will be the subject of further studies combined with powder XRD [21].

The successful demonstration of combined ion and electron beam techniques to investigate the structure of the oxide forming on the metal, will now pave the way for a detailed future study of oxide formation over a range

of environmental conditions and may be equally applied to the study of other metal and alloy systems.

[1] M. M. Baker, L. N. Less, S. Orman, Uranium and water reaction. part 2 effect of oxygen and other gases, Transactions of the Faraday Society 62 (0) (1966) 2525–2530.

[2] S. G. Bazley, J. R. Petherbridge, J. Glascott, The influence of hydrogen pressure and reaction temperature on the initiation of uranium hydride sites, Solid State Ionics 211 (2012) 1–4.

[3] F. H. Spedding, A. S. Newton, J. C. Warf, O. Johnson, R. W. Nottorf, I. B. Johns, A. H. Daane, Uranium hydride 1. preparation, composition and physical properties, Nucleonics 4 (1) (1949) 4–15.

[4] L. W. Owen, R. Scudamor, A microscope study of the initiation of hydrogen-uranium reaction, Corrosion Science 6 (11-1) (1966) 461–466.

[5] R. Arkush, A. Venkert, M. Aizenshtein, S. Zalkind, D. Moreno, M. Brill, M. H. Mintz, N. Shamir, Site related nucleation and growth of hydrides on uranium surfaces, Journal of Alloys and Compounds 244 (1-2) (1996) 197–205.

[6] R. M. Harker, The influence of oxide thickness on the early stages of the massive uranium-hydrogen reaction, Journal of Alloys and Compounds 426 (1-2) (2006) 106–117.

[7] Y. Ben-Eliyahu, M. Brill, M. H. Mintz, Hydride nucleation and formation of hydride growth centers on oxidized metallic surfaces-kinetic theory, Journal of Chemical Physics 111 (13) (1999) 6053–6060.

[8] J. Glascott, A model for the initiation of reaction sites during the uranium-hydrogen reaction assuming enhanced hydrogen transport through thin areas of surface oxide, Philosophical Magazine 94 (3) (2013) 221–241.

[9] L. Baker Jr, J. D. Bingle, The kinetics of oxidation of uranium between 300 and 625 °C, Journal of Nuclear Materials 20 (1) (1966) 11–21.

[10] A. G. Ritchie, The kinetics of the initial stages of the reaction of uranium with oxygen, Journal of the Less Common Metals 98 (2) (1984) 193–214.

[11] A. G. Ritchie, A review of the rates of reaction of uranium with oxygen and water vapour at temperatures up to 300 °C, Journal of Nuclear Materials 102 (1-2) (1981) 170–182.

[12] A. G. Ritchie, The kinetics and mechanism of the uranium-water vapour reaction - an evaluation of some published work, Journal of Nuclear Materials 120 (2) (1984) 143–153.

[13] A. G. Ritchie, R. C. Greenwood, S. J. Randles, The kinetics of the uranium-oxygen-water vapour reaction between 40 and 100 °C, Journal of Nuclear Materials 139 (2) (1986) 121–136.

[14] M. M. Baker, L. N. Less, S. Orman, Uranium and water reaction. Part 1. Kinetics, products and mechanism, Transactions of the Faraday Society 62 (0) (1966) 2513–2524.

[15] G. W. McGillivray, D. A. Geeson, R. C. Greenwood, Studies of the kinetics and mechanism of the oxidation of uranium by dry and moist air - A model for determining the oxidation rate over a wide range of temperatures and water vapour pressures, Journal of Nuclear Materials 208 (12) (1994) 81–97.

[16] J. M. Haschke, T. H. Allen, L. A. Morales, Reactions of plutonium dioxide with water and hydrogen-oxygen mixtures: Mechanisms for corrosion of uranium and plutonium, Journal of Alloys and Compounds 314 (12) (2001) 78–91.

[17] D. T. Larson, Oxidation of a ternary uranium alloy, Journal of Vacuum Science & Technology 8 (1) (1971) 80–83.

[18] S. Lin, X. Lai, X. Lv, H. Zhang, Study of the initial oxidation characteristics of uranium with pure oxygen below 100 °C by spectroscopic ellipsometry, Surface and Interface Analysis 40 (3-4) (2008) 645–648.

[19] W. J. Siekhaus, Composition of uranium oxide surface layers analyzed by μ-raman spectroscopy, MRS Online Proceedings Library 802.

[20] G. C. Allen, P. M. Tucker, R. A. Lewis, X-ray photoelectron spectroscopy study of the initial oxidation of uranium metal in oxygen + water-vapour mixtures, Journal of the Chemical Society, Faraday Transactions 2: Molecular and Chemical Physics 80 (8) (1984) 991–1000.

[21] Z. Chernia, The initial stage of uranium oxidation - mechanism of UO_2 scale formation in the presence of a native lateral stress field., The Journal of Chemical Physics B 110 (46) (2006) 23041–23051.

[22] J. T. Waber, J. A. O'Rourke, R. Kleinberg, Oriented dioxide films on uranium, Journal of The Electrochemical Society 106 (2) (1959) 96–102.

[23] A. Bessonov, B. Borisov, V. Vlasov, Investigation of the structure of primary oxide layer on uranium, The Physics of Metals and Metallography 11.

[24] P. W. Tasker, The surface properties of uranium dioxide, Surface Science 87 (2) (1979) 315–324.

[25] C. P. Jones, T. B. Scott, J. R. Petherbridge, Structural deformation of metallic uranium surrounding hydride growth sites, Corrosion Science 96 (2015) 144–151.

[26] N. J. Harker, T. B. Scott, C. P. Jones, J. R. Petherbridge, J. Glascott, Altering the hydriding behaviour of uranium metal by induced oxide penetration around carbo-nitride inclusions, Solid State Ionics 241 (2013) 46–52.

[27] T. B. Scott, J. R. Petherbridge, N. J. Harker, R. J. Ball, P. J. Heard, J. Glascott, G. C. Allen, The oxidative corrosion of carbide inclusions at the surface of uranium metal during exposure to water vapour, Journal of Hazardous Materials 195 (2011) 115–123.

[28] N. J. Harker, The corrosion of uranium in sealed environments containing oxygen and water vapour, PhD thesis, University of Bristol.

[29] V. K. Orlov, V. S. Sergeev, M. A. Fomishkin, A. A. Rostovtsev, A. K. Kruglov, Carbon diffusion in uranium during thermal reprocessing in vacuum, Atomic Energy 95 (2) (2003) 536–539.

[30] G. C. Allen, P. A. Tempest, Linear ordering of oxygen clusters in hyperstoicheiometric uranium dioxide, Journal of the Chemical Society, Dalton Transactions (11) (1982) 2169–2173.

[31] G. C. Allen, P. A. Tempest, The accommodation of oxygen clusters in hyperstoicheiometric uranium dioxide and its effects on crystal structure, Journal of the Chemical Society, Dalton Transactions (12) (1983) 2673–2677.

[32] V. J. Wheeler, The diffusion and solubility of hydrogen in uranium dioxide single crystals, Journal of Nuclear Materials 40 (2) (1971) 189–194.